Physics in Medicine & Biology

ACCEPTED MANUSCRIPT

The noise navigator for MRI-guided radiotherapy: an independent method to detect physiological motion

To cite this article before publication: Robin J M Navest *et al* 2020 *Phys. Med. Biol.* in press https://doi.org/10.1088/1361-6560/ab8cd8

Manuscript version: Accepted Manuscript

Accepted Manuscript is “the version of the article accepted for publication including all changes made as a result of the peer review process, and which may also include the addition to the article by IOP Publishing of a header, an article ID, a cover sheet and/or an ‘Accepted Manuscript’ watermark, but excluding any other editing, typesetting or other changes made by IOP Publishing and/or its licensors”

This Accepted Manuscript is **© 2020 Institute of Physics and Engineering in Medicine**.

During the embargo period (the 12 month period from the publication of the Version of Record of this article), the Accepted Manuscript is fully protected by copyright and cannot be reused or reposted elsewhere.
As the Version of Record of this article is going to be / has been published on a subscription basis, this Accepted Manuscript is available for reuse under a CC BY-NC-ND 3.0 licence after the 12 month embargo period.

After the embargo period, everyone is permitted to use copy and redistribute this article for non-commercial purposes only, provided that they adhere to all the terms of the licence https://creativecommons.org/licences/by-nc-nd/3.0

Although reasonable endeavours have been taken to obtain all necessary permissions from third parties to include their copyrighted content within this article, their full citation and copyright line may not be present in this Accepted Manuscript version. Before using any content from this article, please refer to the Version of Record on IOPscience once published for full citation and copyright details, as permissions will likely be required. All third party content is fully copyright protected, unless specifically stated otherwise in the figure caption in the Version of Record.

View the article online for updates and enhancements.

This content was downloaded from IP address 129.180.1.217 on 26/04/2020 at 01:01

The noise navigator for MRI-guided radiotherapy: an independent method to detect physiological motion

R.J.M. Navest[1,2], **S. Mandija**[1,2], **S.E. Zijlema**[1,2] **B. Stemkens**[1,2], **A. Andreychenko**[1,3], **J.J.W. Lagendijk**[1] **and C.A.T. van den Berg**[1,2]

[1] Department of Radiotherapy, University Medical Center Utrecht, Utrecht, Netherlands

[2] Computational Imaging Group for MRI Diagnostics & Therapy, Centre for Image Sciences, Universiy Medical Center Utrecht, Utrecht, Netherlands

[3] Research and Practical Clinical Center of Diagnostics and Telemedicine Technologies, Department of Health Care of Moscow, Moscow, Russian Federation

E-mail: `r.j.m.navest@umcutrecht.nl`

Abstract. Motion is problematic during radiotherapy as it could lead to potential underdosage of the tumor, and/or overdosage in organs-at-risk. A solution is adaptive radiotherapy guided by magnetic resonance imaging (MRI). MRI allows for imaging of target volumes and organs-at-risk before and during treatment delivery with superb soft tissue contrast in any desired orientation, enabling motion management by means of (real-time) adaptive radiotherapy.

The noise navigator, which is independent of the MR signal, could serve as a secondary motion detection method in synergy with MR imaging. The feasibility of respiratory motion detection by means of the noise navigator was demonstrated previously. Furthermore, from electromagnetic simulations we know that the noise navigator is sensitive to tissue displacement and thus could in principle be used for the detection of various types of motion.

In this study we demonstrate the detection of various types of motion for three anatomical use cases of MRI-guided radiotherapy, i.e. torso (bulk movement and variable breathing), head-and-neck (swallowing) and cardiac. Furthermore, it is shown that the noise navigator can detect bulk movement, variable breathing and swallowing on a hybrid 1.5T MRI-linac system. Cardiac activity detection through the noise navigator seems feasible in an MRI-guided radiotherapy setting, but needs further optimization. The noise navigator is a versatile and fast (millisecond temporal resolution) motion detection method independent of MR signal that could serve as an independent verification method to detect the occurrence of motion in synergy with real-time MRI-guided radiotherapy.

Keywords: Physiological motion, Magnetic Resonance Imaging, Radiotherapy, Noise navigator, Thermal noise

Introduction

Motion is problematic during radiotherapy as it could lead to potential underdosage of the tumor, and/or overdosage in organs-at-risk (OARs). A solution is adaptive radiotherapy guided by magnetic resonance imaging (MRI). Currently, there are two clinically used MRI-guided radiotherapy (MRIgRT) systems that combine an MRI scanner with a radiation therapy unit (Lagendijk et al. 2014, Mutic & Dempsey 2014). MRI allows for imaging of target volumes and OARs before and during treatment delivery with superb soft tissue contrast in any desired orientation (Chin et al. 2019), enabling motion management by means of (real-time) adaptive radiotherapy.

Organ displacement due to involuntary (e.g. cardiac motion) or sudden voluntary motion (e.g. bulk body movements or swallowing) can occur during treatment delivery. Beam-on MR images could visualize these organ displacements and facilitate real-time motion management techniques, such as exception gating (e.g. stopping treatment during bulk body movement or swallowing), repetitive gating (e.g. for respiratory or cardiac motion), and potentially tumor tracking (van Herk et al. 2018). These real-time MRIgRT motion management techniques, however, would require MRI with minimal imaging latency (Borman et al. 2018). Currently, the time required to acquire a full 3D MRI volume (order of seconds) is too slow for real-time applications. Fast 2D cine MR images could be used to measure motion (Koch et al. 2004), but this approach makes it difficult to track through-plane motion. A solution to both problems is to use a motion model (McClelland et al. 2013), driven by fast 2D MR images, that estimates the full 3D motion (McClelland et al. 2017, Fayad et al. 2012, Harris et al. 2016, Stemkens et al. 2016, Garau et al. 2019, Paganelli et al. 2019). The validity of these motion models over time, however, is not guaranteed and would ideally be tested regularly with an independent motion detection method.

The noise navigator (Andreychenko et al. 2017, Navest, Andreychenko, Lagendijk & van den Berg 2018) could serve as such a secondary motion detection method independent of the MR signal. The noise navigator originates from the inherently present thermal noise measured by a radiofrequency (RF) receive coil and thus is independent from the imaging volume or contrast of the MR images. Moreover, the noise navigator could be acquired during MRI, but motion could also be detected by silent passive noise measurements during periods MRI is not typically acquired (e.g. recontouring for MRIgRT) (Stemkens et al. 2018, Paganelli et al. 2018). Finally, the noise navigator can be acquired on a much faster (millisecond) time scale than MR images.

The feasibility of respiratory motion detection by means of the noise navigator has been demonstrated in a diagnostic MRI setting (Andreychenko et al. 2017, Navest, Andreychenko, Lagendijk & van den Berg 2018). Furthermore, the noise navigator could be used as respiratory motion surrogate for 4D-MRI generation in an MRI simulation for radiotherapy setting (Navest et al. 2020). In this work we took the next step to demonstrate the feasibility of the noise navigator as a secondary means to detect the occurrence of motion for MRI-guided radiotherapy. With the application of MRI-guided radiotherapy in mind, it would be desirable to detect any occurrence of motion. From our previous work that investigated the physical origins of the noise navigator (Navest et al. 2019), we know that the noise navigator in principle can detect (i.e. qualitatively measure) the occurrence of tissue displacement and thus is not limited to the detection of respiratory motion. To investigate the feasibility of detecting the occurrence of motion other than respiration, three different use cases that are relevant for MRI-guided radiotherapy (i.e. torso, head-and-neck and cardiac) were investigated in an MRI-guided radiotherapy setup. The cardiac use case can be seen as part of the torso, but will be addressed separately since it is especially challenging to detect cardiac motion due to the relatively fast yet subtle motion involved.

Torso use case

In the torso, the three principal sources of motion are the beating heart, breathing and bulk body movement (van Heeswijk et al. 2012). Previously, we have demonstrated the feasibility of regular breathing detection using the noise navigator (Andreychenko et al. 2017, Navest, Andreychenko, Lagendijk & van den Berg 2018) and subsequent respiratory-correlated 4D-MRI generation (Navest et al. 2020). Here, we will focus on variable breathing and simultaneous breathing and bulk movement detection in a clinical setup on a hybrid MRI-linac system.

Head-and-neck use case

For HN radiotherapy, it is common practice to restrict motion with immobilization devices such as thermoplastic masks (Nakata et al. 2013) and a personalized head support (Houweling et al. 2010). Nevertheless, internal motion like swallowing cannot be restricted with immobilization devices and swallowing-induced motion of HN tumors are relatively large, i.e. 15-29 mm (Leonard et al. 2000, van Asselen et al. 2003, Prévost et al. 2008, Dantas et al. 1990, Jacob et al. 1989, Bradley et al. 2011, Hamlet et al. 1994, Bruijnen et al. 2019). Hence, the feasibility of swallowing event detection was investigated on a hybrid MRI-linac system.

Cardiac use case

The electrocardiogram (ECG) is currently the best method for cardiac activity detection. The ECG signal, however, can be disturbed by the magnetohydrodynamic effect (Jekic et al. 2010) and requires careful placement of ECG electrodes leading to longer patient setup times. Moreover, these ECG skin electrodes and cables could interfere with radiation dose delivery and thus cannot be used during MRIgRT. The noise navigator, on the other hand, does not require additional hardware and should in principle be sensitive to cardiac activity as shown in our previous electromagnetic simulation study (Navest et al. 2019). The feasibility of cardiac activity detection by means of the noise navigator was investigated in the context of MRIgRT.

Methods

MR experiments

Prior to the measurements, all volunteers signed a written informed consent approved by the institutional review board. All volunteers were between 22 and 34 years old and had a body mass index between 18.5 and 25.5.

Torso use case Ten healthy volunteers were scanned on a 1.5T MRI-linac system (Unity, Elekta AB, Stockholm, Sweden). Signal was collected with a clinically used MRI-linac RF receive array consisting of a four channel posterior array located under the table and four channel anterior array attached to a coil bridge (see Figure 1 A). This setup was used for bulk movement and variable breathing detection. A 2D balanced steady-state free precession cine MRI (50° flip angle, 3.4 ms TR, 1.7 ms TE, 2x2 mm^2 voxels, 280x560 mm^2 field-of-view, 7 mm slice thickness, 0.625 halfscan, SENSE 1.6, and 1 MHz receive bandwidth) was continuously acquired for 350 repetitions (186 ms temporal resolution). For bulk movement detection the 2D cine MRI slice was placed transversally, whereas for variable breathing detection the slice was positioned sagittally through the liver and right kidney. A total of sixty experiments were performed. Each volunteer performed two experiments in which sudden bulk movement (e.g. due to patient discomfort) was simulated. Additionally, four experiments with variable breathing, i.e. two with a variable breathing frequency and two experiments where the volunteers were asked to switch between an abdominal and thoracic breathing pattern.

Head-and-neck use case Ten healthy volunteers were scanned on a 1.5T MRI-linac system with a single flexible experimental radiolucent high-impedance RF receive coil (Zhang et al. 2018, Zijlema, Tijssen, Malkov, van Dijk, Hackett, Kok, Lagendijk & van den Berg 2019) of 19 cm length and 7 cm width (see Figure 1 B). This single coil was connected to the MR scanner via an in-house developed interfacing box that contained the preamplification and digitization hardware. For swallowing detection, this coil was positioned on the neck with a velcro strap (see Figure 1 C). A sagittal 2D T1-weighted RF-spoiled incoherent gradient echo cine MRI (4° flip angle, 4.6 ms TR, 2.2 ms TE, 2x2 mm^2 voxels, 150x560 mm^2 field-of-view, 10 mm slice thickness, 0.625 halfscan, and 427 kHz receive bandwidth), positioned through the larynx, was continuously acquired for 200 repetitions (216 ms temporal resolution). A total of seventeen experiments were performed in which the volunteer was instructed to swallow two or three times.

Cardiac use case Noise-only experiments were performed on five healthy volunteers (three male and two female) on a clinical 1.5T MRI scanner (Ingenia MR-RT system, Philips, Best, The Netherlands) with a single radiolucent high-impedance RF receive coil fixated at 2 cm to the left of the sternum using a velcro strap (see Figure 1 D). The detection of cardiac activity was validated with simultaneous ECG monitoring on an MRI scanner, because the ECG signal could not be acquired on the used MRI-linac system. The noise-only acquisitions were measured with a balanced steady-state free precession sequence (2.47 ms TR and 1 MHz receive bandwidth) where the gradients and RF-excitation were turned off. A total of twenty experiments were performed. Two noise-only measurements were performed during breath hold (18 s duration) and two during free breathing (60 s duration).

Noise navigator calculation

The thermal noise variance was calculated per readout (NN_1) using the complex k-space signal measured by each channel in the clinically used MRI-linac RF receive array or the high-impedance RF receive coil (Navest, Andreychenko, Lagendijk & van den Berg 2018). For the combination of the channels in the clinically used MRI-linac RF receive array, a principal component analysis was performed over these receive channels. For breathing detection, the principal component with the highest power in the respiratory frequency band 0.05 to 0.8 Hz (i.e. 3 to 48 breaths/min) was selected (Navest, Andreychenko, Lagendijk & van den Berg 2018). For simultaneous bulk movement and breathing detection, the principal component with the highest power between 0 and 0.8 Hz was chosen. For an overview of the noise navigator calculations per use case see supplementary material 1.

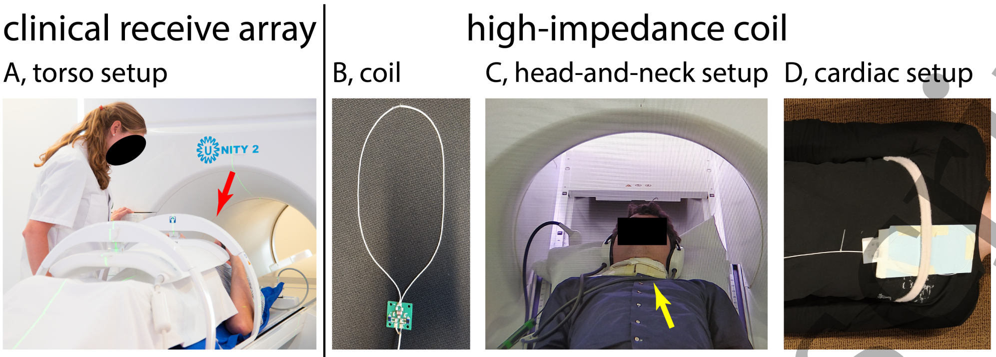

[redacted]

[redacted]

Figure 1. The torso setup with the clinically used MRI-linac RF receive array (A), where the coil bridge is indicated by a red arrow. In B, the high-impedance coil is depicted without any protective material. The head-and-neck and cardiac measurement setup with the high-impedance coil are shown in C and D, respectively.

Noise navigator post-processing

Prospective applications typically require a minimum latency for acquisition and processing. With the application of MRIgRT in mind, processing latencies were minimized by applying a Kalman filter (Kalman 1960) to NN_1. Additionally, for the torso and HN use cases, the average unfiltered noise navigator value per cine MR image (NN_{im}) was calculated as a general comparison to the cine MR images.

Torso use case A Kalman filter designed to predict respiratory motion (Navest, Andreychenko, Lagendijk & van den Berg 2018) was applied to NN_1 to detect motion per readout (i.e. 3.4 ms temporal resolution).

Head-and-neck use case The average thermal noise variance over ten readouts (NN_{10}) was calculated, resulting in a temporal resolution of 46 ms. Subsequently, a Kalman filter with random walk model (Mulquiney et al. 1995) was used to smoothen the signal.

Cardiac use case Two separate parallel Kalman filters were applied to NN_1 (i.e. 2.5 ms temporal resolution). One Kalman filter extracted the cardiac activity between 0.7 and 1.4 Hz (i.e. 42 and 84 beats per minute) while the other was specific to detect the breathing signal (Navest, Andreychenko, Lagendijk & van den Berg 2018).

MRI-based displacement calculation

For validation, deformation vector fields (DVFs) were calculated with an optical flow algorithm (Zachiu, Papadakis, Ries, Moonen & Denis de Senneville 2015, Zachiu, Denis de Senneville, Moonen & Ries 2015) applied to the 2D cine MR images in the torso and HN use cases. Optical flow was chosen, because this method has already been validated and used for torso (Zachiu, Papadakis, Ries, Moonen & Denis de Senneville 2015) and head-and-neck (Bruijnen et al. 2019) anatomical sites. To compare the DVFs and the noise navigator, the mean displacement within a region-of-interest (ROI) was calculated.

The ROI depended on the motion of interest. The full anatomy was selected for the transversally positioned torso MR images for simultaneous bulk body movement and respiration detection. Only the top half of the liver was selected for the sagittal torso MR images used for respiratory motion detection. Finally, an ROI containing the larynx was selected for swallowing detection in the HN use case.

Motion detection validation

2D cine MR images The correlation and Kullback–Leibler (KL) convergence (Kullback & Leibler 1951) between NN_{im} and the MRI-based displacement was calculated to serve as a general comparison for the torso and HN use cases. Additionally, the correlation and KL convergence between the Kalman-filtered noise navigator (i.e. NN_1 for the torso and NN_{10} for the HN use case) and MRI-based displacement were calculated after linearly interpolating the Kalman-filtered noise navigator to match the time samples of the MRI-based displacement.

For swallowing event detection in the HN use case, thresholding of the Kalman-filtered NN_{10} was performed. The thermal noise variance threshold of 1.8% was empirically determined over a total of seventeen measurements on ten subjects. The events detected by the Kalman-filtered NN_{10} with this threshold and the MRI-based displacement were compared.

ECG For the cardiac use case, the Kalman-filtered NN_1 was validated against the simultaneously acquired ECG signal in both the frequency and temporal domain.

Trigger signals were calculated by performing peak detection on the noise navigator and ECG. The stability of the noise navigator trigger signal was evaluated by calculating the standard deviation of the time difference between the triggers provided by the noise navigator and ECG. Furthermore, the cross-correlation between the two trigger signals was calculate to obtain the trigger delay.

Results

Torso use case

Figure 2 shows the MRI-based displacement and noise navigator for an experiment where the breathing frequency varied over time. Notice that NN_{im} and MRI-based displacement are very similar. Furthermore, the mean absolute correlation between these two was 0.93 over all volunteer measurements. All absolute correlations were in the range 0.66 to 0.96 (see supplementary material 2). Similarly, the Kalman-filtered NN_1, with an approximately 55 times higher temporal resolution than the 2D cine MRI, had a good mean absolute correlation of 0.88 with the MRI-based displacement (range 0.56 to 0.93). Furthermore, all KL convergence with respect to the MRI-based displacement was below 0.12 and 0.2 for NN_{im} and NN_1, respectively (see supplementary material 3). The only discrepancy observed between the Kalman-filtered NN_1 and the MRI-based displacement is the negative baseline shift between 13 and 20 seconds, that is not detected by the Kalman-filtered NN_1. The MR images corresponding to the encircled numbers next to the curves indicate exhale, inhale and deep inhale in increasing order. The yellow line in the MR images shows the position of the liver dome in exhale. See supplementary material A1 for an animated figure of this measurement. Additionally, supplementary material A2 shows an animated figure of a measurement in which the volunteer performed thoracic breathing during the first thirty seconds and afterwards continued with abdominal breathing.

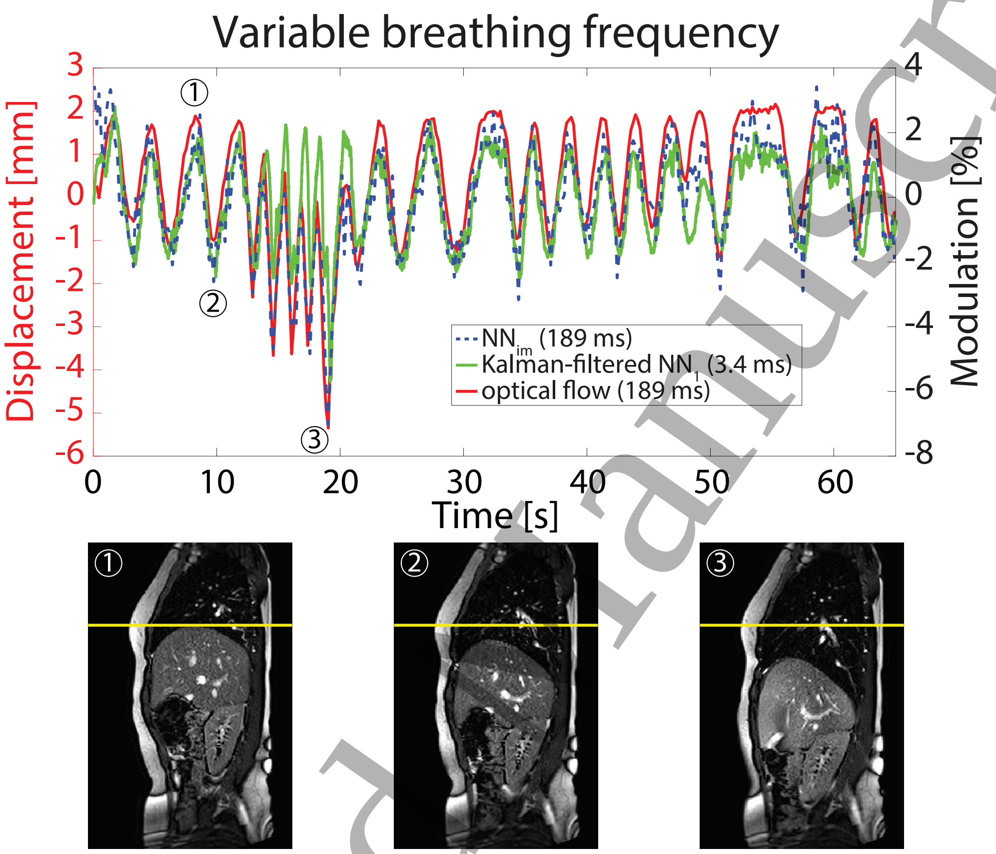

Figure 2. Representative volunteer measurements containing a variable breathing frequency. The temporal resolution is indicated in the legend. The optical flow (red) and NN_{im} (dashed blue) were calculated per cine MR image. By applying a Kalman filter per readout (green), a 55 times higher temporal resolution could be achieved for the noise navigator. The encircled numbers indicate the time point depicted in the corresponding MR images.

Figure 3 shows that the noise navigator can be simultaneously used to detect respiration, as demonstrated by the periodic modulation, and bulk movement (at 19 seconds). Moreover, the different positions of the body before and after the bulk body shift were detected by the noise navigator and could be independently observed in the MR images corresponding to the encircled numbers next to the curves. Note that there is through-plane motion, a slightly different contrast, and image masking (on the left of MR image 3) as a result of the bulk motion. See supplementary material A3 for an animated figure of this measurement. The mean absolute correlation between the NN_{im} and MRI-based displacement was 0.85. All absolute correlations were in the range 0.74 to 0.99 (see supplementary material 2). Furthermore, all KL convergence were between 0.002 and 0.34, with a mean of 0.05 (see supplementary material 3). Similarly, a mean absolute correlation of 0.71 (range 0.65 to 0.98) was found between the Kalman-filtered NN_1 and MRI-based displacement. Additionally, a mean KL convergence of 0.07 (range from 0 to 0.52) was found. The largest discrepancies between the MRI-based displacement and Kalman-filtered NN_1 were observed immediately after a bulk movement event (e.g. Figure 3 between 19 and 20 seconds).

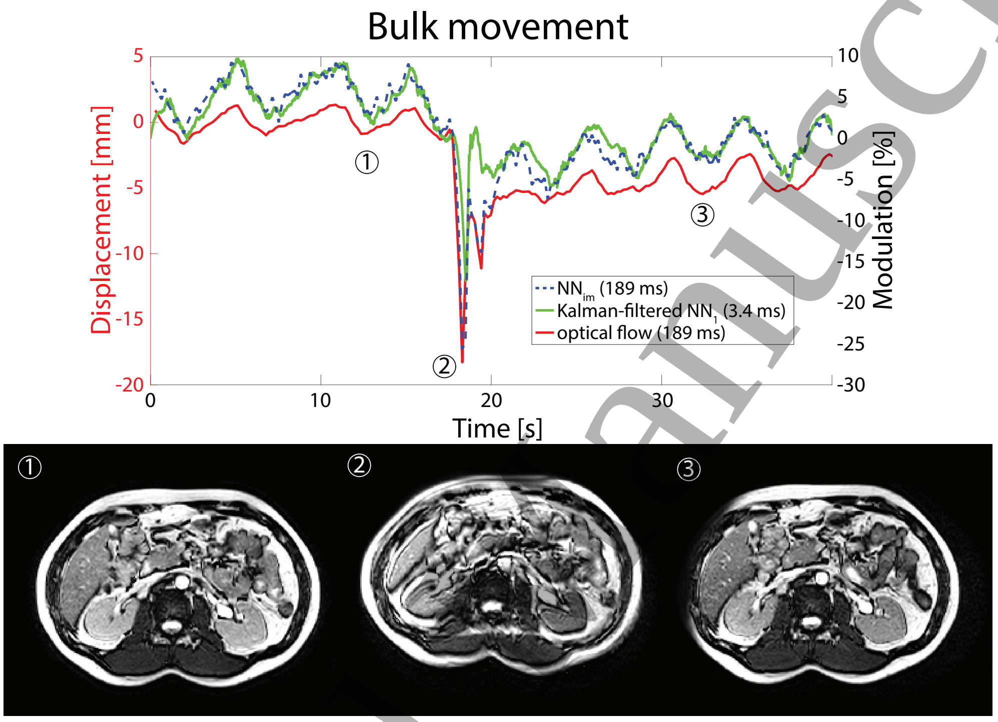

Figure 3. An example of bulk movement detection containing a bulk body shift on a healthy volunteer. The temporal resolution is indicated in the legend. The optical flow (red) and NN_{im} (dashed blue) were calculated per cine MR image. By applying a Kalman filter per readout (green), a 55 times higher temporal resolution could be achieved for the noise navigator. The encircled numbers indicate the time point depicted in the corresponding MR images.

Head-and-neck use case

Figure 4 shows a representative volunteer measurement, containing two swallowing events, performed with a high-impedance RF receive coil. Notice that NN_{im} and the Kalman-filtered NN_{10} agree well. With a simple threshold (dashed magenta line), 92% of all 38 swallowing events were correctly detected based on the Kalman-filtered NN_{10}. In addition to the correctly detected swallowing events, six false-positives were detected and three swallowing events were not detected. The MR images corresponding to the encircled numbers next to the curves indicate the onset and maximum larynx displacement of a swallowing event in increasing order. Notice the inferior image quality in the back of the neck caused by the larger distance of the anatomy to the single receive coil. See supplementary material A4 for an animated figure. Additionally, see supplementary material 4 for swallowing detection examples in six other volunteers.

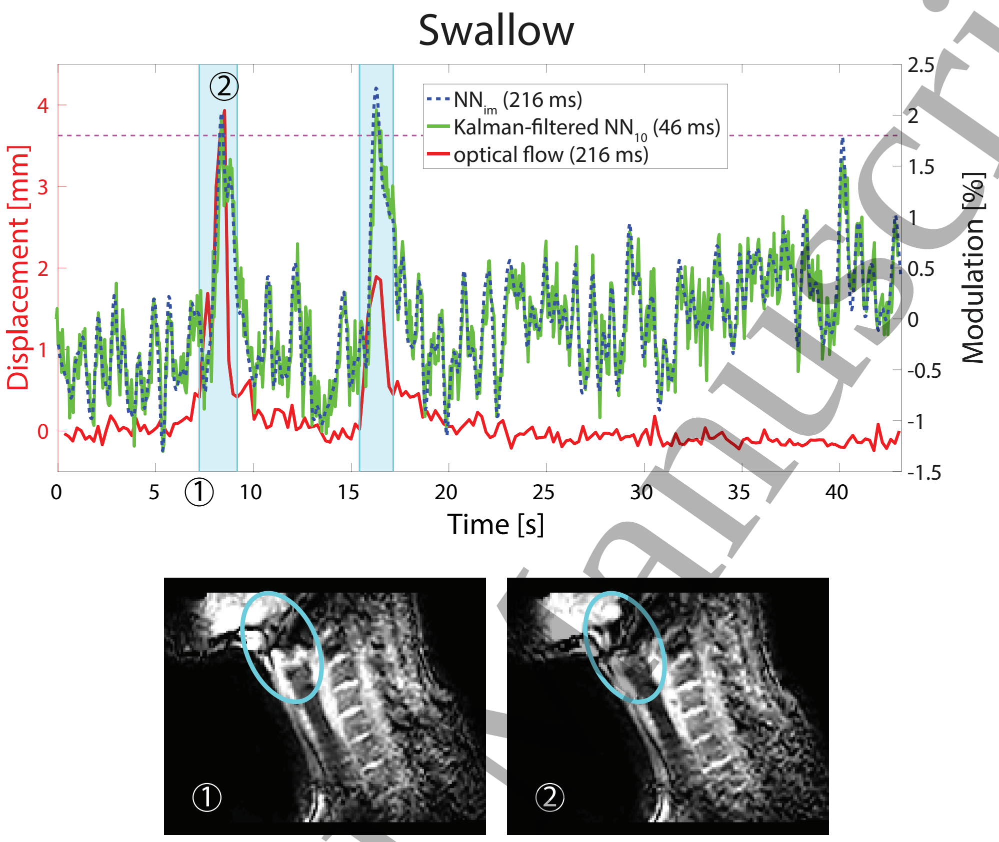

Figure 4. A representative swallowing detection example on a healthy volunteer. The cyan rectangles indicate the swallowing events and the horizontal dashed magenta line indicates the thermal noise variance threshold. The temporal resolution is indicated in the legend. The optical flow (red) and NN_{im} (dashed blue) were calculated per cine MR image. By applying a Kalman filter per 10 readouts (green), a 4 times higher temporal resolution could be achieved for the noise navigator. The encircled numbers indicate the time point depicted in the corresponding MR images.

The correlation between NN_{im} and the MRI-based displacement was in the range of 0.06 and 0.75, with a mean value of 0.37 (see supplementary material 2). The NN_{10} with an approximately five times higher temporal resolution yielded a similar mean correlation of 0.36 (range between 0.08 and 0.77). All KL convergence with respect to the MRI-based displacement was below 0.07 and 0.06 for NN_{im} and NN_{10}, respectively (see supplementary material 3).

Cardiac use case

In Figure 5 A, the spectral peak related to cardiac and respiratory motion detected with a high-impedance RF receive coil can be seen in the unfiltered NN_1 frequency spectrum at 0.76 Hz (i.e. 45.6 beats per minute) and 0.24 Hz (i.e. 14.4 breaths per minute), respectively. Notice that amplitudes of the detected cardiac activity (i.e. 1.6) and respiration (i.e. 1.5) are comparable. A good match between the noise navigator and ECG signal was observed (see Figure 5 B). Additionally, respiration (see Figure 5 C) could be extracted simultaneously with cardiac activity. For another example of simultaneous cardiac and respiratory motion detection in a different volunteer see supplementary material 5.

Cardiac activity could be detected for all three male volunteers during breath hold (see supplementary material 6). During free breathing, cardiac activity and respiration was observed in two male volunteers and only respiration was observed in the other male volunteer. In the female volunteers cardiac activity could not be detected with the noise navigator (see supplementary material 7).

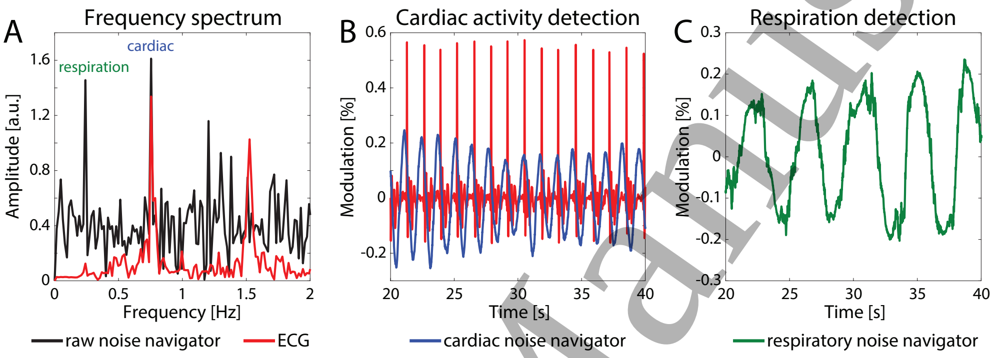

Figure 5. An example free breathing experiment on one of the healthy male volunteers. The frequency spectrum (A) shows both cardiac and respiratory motion in the unfiltered NN_1. The cardiac NN_1 shows a peak just before the R-top in the ECG (B). In C the breathing extracted from NN_1 is shown.

A mean standard deviation of 0.28 seconds (range between 0.23 and 0.32) was found for the time difference between triggers based on the noise navigator and ECG in breath hold. During free breathing experiments the standard deviation was between 0.33 and 0.42 (mean 0.37 seconds). A mean trigger delay of 0.2 seconds was found for the breath hold experiments with a range between 0.01 and 0.57 seconds. Furthermore, a trigger delay between -0.77 and 0.07 seconds with a mean of -0.28 seconds was found during free breathing experiments.

Discussion

We investigated the use of the noise navigator for the detection of different types of motion for three anatomical use cases of MRIgRT, i.e. torso, head-and-neck and cardiac. In this study it was shown that the noise navigator can be used as an independent verification method to detect the occurrence of physiological motion with a subsecond resolution in an MRI-guided radiotherapy setting.

We do not foresee that the noise navigator can replace MR imaging as guidance modality, but it could serve a role in a number of applications of MRIgRT. Although online 3D MR imaging provides superior guidance of radiotherapy, it comes with some downsides. 3D acquisitions are inherently time-consuming and the 3D reconstruction process adds even more time (latency). As a consequence, at least several seconds are typically required to obtain 3D motion information. Motion occurring within this acquisition window will result in motion artifacts in the 3D images. The synergy of the noise navigator with MRI stems from the fact that the occurrence of motion can be detected on a much faster time scale. Furthermore, in the case of online 3D motion tracking using a 3D motion model (McClelland et al. 2017, Fayad et al. 2012, Harris et al. 2016, Stemkens et al. 2016, Garau et al. 2019, Paganelli et al. 2019), the validity of the motion model might be constantly verified with the noise navigator. Additionally, the noise navigator could be utilized to monitor physiological functions, such as respiration and cardiac rates during therapy, and provide e.g. an independent secondary trigger signal for exception gating.

In line with this, the ability of the noise navigator to detect motion on a readout basis offers the potential to reduce the impact of motion artifacts in diagnostic MR images. For instance the detection of movements with a short duration, like swallowing, could be used to discard readouts corrupted by motion that would deteriorate image quality (Navest, Bruijnen, Lagendijk, Andreychenko & van den Berg 2018).

The main benefit of the noise navigator comes from the fact that it provides a secondary means to detect motion. An additional useful quality of the noise navigator is that it comes for free during MR signal reception or can be acquired separately using passive, silent noise-only measurements (without gradient operation and RF excitation). This could be exploited for instance during recontouring/replanning where silent passive noise measurements could be used to detect whether the patient has moved and new MR imaging is required.

For these purposes, however, the demonstrated detection of the occurrence of various types of motion requires further results to prove robust use of the noise navigator in an MRIgRT setting. Nevertheless we believe that this study provides a proof-of-principle.

Torso use case

We have demonstrated a good correlation and KL convergence between the MRI-based displacement and NN_{im} for a total of sixty experiments, including bulk movement and variable breathing, in ten healthy volunteers on a hybrid MRI-linac system. Furthermore, a Kalman filter was applied to NN_1, which allowed for motion detection approximately 55 times faster than with the 2D cine MR images used for validation. With this Kalman filter, however, it is possible that a sudden displacement shift (e.g. see Figure 2 A between 13 and 20 seconds) is underestimated because it is currently not described by the model driving the Kalman filter predictions. Moreover, the used respiratory motion model (i.e. a sine wave) underlying the Kalman filter prediction does in principle not properly describe bulk movement. This resulted in discrepancies between the Kalman-filtered NN_1 and MRI-based displacement immediately after a bulk motion event (e.g. Figure 3 between 19 and 20 seconds). Nevertheless, both breathing and sudden bulk movement could be detected by the Kalman-filtered NN_1.

Accurate respiratory motion detection even continued after the occurrence of bulk movement indicating the robustness of the method. Note that after a bulk body shift, the baseline signal of the noise navigator was lowered indicating that the body position is different from the initial position (see Figure 3). This is also confirmed by the MR images. Thus, monitoring of the noise navigator could potentially provide a simple and high temporal means to qualitatively detect gradual drift in body position.

Head-and-neck use case

Swallowing detection was not feasible with the clinically used MRI-linac RF receive array (data not shown here), because of the elevated coil setup, similar to Figure 1 A, and relatively large coils (i.e. approximately 45 cm length and 13 cm width). With a smaller radiolucent high-impedance RF receive coil (i.e. 19 cm length and 7 cm width), which is closer to the anatomy of interest it was possible to detect swallowing events through the noise navigator visually.

The mean correlation between the MRI-based displacement and the noise navigator (i.e. NN_{im} and NN_{10}) was relatively low due to the random fluctuations in the baseline when no swallowing event occurred. The KL convergence showed a good correspondence between NN_{im} and NN_{10} and the MRI-based displacement. Moreover, combined with a simple thresholding method, 92% of all swallowing events could be detected automatically.

The drift observed after 20 seconds in Figure 4, is most likely physiologic as it was not observed in all volunteers (see supplementary material 4 for more examples). Furthermore, a noise-only acquisition was performed on a solid static phantom for 32 minutes in which no drift was observed (see supplementary material 8).

We are convinced that in combination with a dedicated HN receive array made up of high-impedance coils (Ruytenberg et al. 2018, Zijlema, van Dijk, Gotby, Italiaander, Tijssen, Lagendijk & van den Berg 2019), swallowing detection through the noise navigator would be feasible in a clinical setup on an MRI-linac system. The swallowing detection sensitivity would be increased by exploiting the additional information of multiple RF receive channels around the neck in such a setup. In addition to an improved measurement setup, the post-processing could be optimized. The Kalman filter predictions could be improved by replacing the random walk model by a model that better describes the motion. Furthermore, it might be worthwhile to explore the possibility of replacing the Kalman filter by time series forecasting using recurrent neural networks (Zhang et al. 1998).

Cardiac use case

It was feasible to detect cardiac activity during breath hold in all three males, but failed in both female volunteers. It is hypothesized that a lower cardiac activity imprint in the noise navigator for females is caused by the larger distance between the coil and the heart due to the presence of breast tissue. As the coil position with respect to the heart was optimized on a single male volunteer, repeating this for a female could yield improved results.

During free breathing, cardiac activity could be detected in two out of three male volunteers. In the third volunteer only respiration was visible. The respiratory motion imprint in the noise navigator is typically a factor ten higher than the cardiac imprint, which makes it challenging to detect cardiac activity in the presence of breathing. Nevertheless, based on these initial results, we believe that cardiac activity detection with the noise navigator is possible. Currently, however, interference between respiration and cardiac-induced modulation in the thermal noise, causes amplitude variations and timing variations between the noise navigator and the ECG signal (see Figure 5 B). This is supported by the relatively high standard deviation observed on the time difference between triggers based on the noise navigator and ECG. It could be speculated that respiration during the cardiac activity detection experiment does affect the noise navigator. Note, however, that there is a large spread in trigger delay values. Due to the relatively low amount of measurements, it is not possible to derive a statistically significant conclusion from these values.

We believe that improved processing (e.g. using time series forecasting using recurrent neural networks) and a measurement setup with multiple RF receive channels could enhance the separation between cardiac and respiration induced modulations. Moreover, the additional information provided by the noise covariances of receive array channels close to the heart will be investigated as this can enhance the spatial sensitivity in the heart (Navest et al. 2019) and minimize thermal noise modulation from other spatial body regions. Here, we showed the cardiac activity detection feasibility with a single high-impedance coil. The noise navigator, however, is not restricted to this type of coil. The experiment at the MRI scanner was repeated on one of the male volunteers with a clinically used traditional (low-impedance) 10 cm diameter loop coil provided by the vendor and cardiac activity was observed in this case too.

Noise navigator limitations

The stochastic nature of the noise navigator could be a limitation. Generally, depending on the application, a compromise between temporal resolution and thermal noise variance estimation accuracy has to be made. The variance estimation precision increases with the square root of the number of samples (Navest, Andreychenko, Lagendijk & van den Berg 2018). A higher precision for variance estimation can be achieved by combining the thermal noise samples of multiple readouts at the cost of temporal resolution. This compromise could be avoided by using the pilot tone navigator (Vahle et al. 2020). The underlying physics of the noise navigator and pilot tone navigator are identical, the only difference is that the pilot tone navigator uses active signal generation whereas the noise navigator utilizes the passive thermal noise. Hence, it is expected that the various types of motion that can be detected with the noise navigator could be detected with the pilot tone navigator too. The active signal generation required for the pilot tone navigator, however, requires additional dedicated hardware and careful calibration to prevent interference with MR imaging.

The main limitation of the noise navigator (and pilot tone navigator), however, is the lack of quantitative displacement information provided by the noise navigator. This problem could be overcome with a (direct correspondence) motion model (McClelland et al. 2013) that converts the noise navigator modulation to displacement. In principle the noise navigator could be extended from the current implementation to a more general concept where instead the noise covariance matrix adds spatial selectivity and sensitivity due to the different physical locations of the channels within an RF receive array (Navest et al. 2019). The feasibility of 2D respiratory liver motion estimation with a linear motion model that uses the temporal behavior of the thermal noise covariance matrix as motion surrogate has already been shown (Andreychenko et al. 2018).

Motion evaluation

In the torso and HN use cases, an optical flow algorithm applied to 2D cine MR images was used as ground truth for motion evaluation. These 2D cine MR images capture the physiological motion of interest when positioned correctly with a sufficient temporal resolution. However, this method assumes that all image intensity variations are caused by displacement within the image. This assumption is not valid in cases with through-plane motion (e.g. respiratory motion for transversal images). Furthermore, during swallowing a saliva bolus, which is hyperintense in the T1-weighted cine MR images, passes through the throat. Even though the assumption of preservation of image intensity is violated, it is still possible to detect motion. The quantification of motion, however, could be under- or overestimated.

Conclusion

The noise navigator can detect bulk movement, variable breathing and swallowing on a hybrid MRI-linac system. Cardiac activity detection through the noise navigator seems feasible in MRI-guided radiotherapy setting, but needs further optimization. The noise navigator is a versatile and fast (millisecond temporal resolution) motion detection method independent of MR signal that could provide additional independent information about the occurrence of a variety of motion types in synergy with MRI for MRI-guided radiotherapy.

Acknowledgments

The authors have confirmed that any identifiable participants in this study have given their consent for publication.

References

Andreychenko A, Denis de Senneville B, Navest R, Tijssen R, Lagendijk J & van den Berg C 2018 *Magnetic Resonance in Medicine* **79**(3), 1730–1735.

Andreychenko A, Raaijmakers A, Sbrizzi A, Crijns S, Lagendijk J, Luijten P & van den Berg C 2017 *Magnetic Resonance in Medicine* **77**(1), 221–228.

Borman P T S, Tijssen R H N, Bos C, Moonen C T W, Raaymakers B W & Glitzner M 2018 *Physics in Medicine & Biology* **63**(15), 155023.

Bradley J A, Paulson E S, Ahunbay E, Schultz C, Li X A & Wang D 2011 *International Journal of Radiation Oncology*Biology*Physics* **81**(5), e803—-e812.

Bruijnen T, Stemkens B, Terhaard C H J, Lagendijk J J W, Raaijmakers C P J & Tijssen R H N 2019 *Radiotherapy and Oncology* **130**, 82–88.

Chin S, Eccles C L, McWilliam A, Chuter R, Walker E, Whitehurst P, Berresford J, Van Herk M, Hoskin P J & Choudhury A 2019 *Journal of Medical Imaging and Radiation Oncology* pp. 1754—-9485.12968.

Dantas R O, Kern M K, Massey B T, Dodds W J, Kahrilas P J, Brasseur J G, Cook I J & Lang I M 1990 *American Journal of Physiology-Gastrointestinal and Liver Physiology* **258**(5), G675—-G681.

Fayad H J, Buerger C, Tsoumpas C, Cheze-Le-Rest C & Visvikis D 2012 *in* '2012 IEEE Nuclear Science Symposium and Medical Imaging Conference Record (NSS/MIC)' IEEE pp. 4058–4061.

Garau N, Via R, Meschini G, Lee D, Keall P, Riboldi M, Baroni G & Paganelli C 2019 *Physics in Medicine & Biology* **64**(4), 045002.

Hamlet S, Ezzell G & Aref A 1994 *International Journal of Radiation Oncology*Biology*Physics* **28**(2), 467–470.

Harris W, Ren L, Cai J, Zhang Y, Chang Z & Yin F F 2016 *International Journal of Radiation Oncology*Biology*Physics* **95**(2), 844–853.

Houweling A C, van der Meer S, van der Wal E, Terhaard C H J & Raaijmakers C P J 2010 *Radiotherapy and Oncology* **96**(1), 100–103.

Jacob P, Kahrilas P J, Logemann J A, Shah V & Ha T 1989 *Gastroenterology* **97**(6), 1469–1478.

Jekic M, Ding Y, Dzwonczyk R, Burns P, Raman S V & Simonetti O P 2010 *Magnetic Resonance in Medicine* **64**(6), 1586–1591.

Kalman R E 1960 *Journal of Basic Engineering* **82**(1), 35.

Koch N, Liu H, Starkschall G, Jacobson M, Forster K, Liao Z, Komaki R & Stevens C W 2004 *International Journal of Radiation Oncology*Biology*Physics* **60**(5), 1459–1472.

Kullback S & Leibler R A 1951 *The Annals of Mathematical Statistics* **22**(1), 79–86.

Lagendijk J J, Raaymakers B W & van Vulpen M 2014 *Seminars in Radiation Oncology* **24**(3), 207–209.

Leonard R J, Kendall K A, McKenzie S, Gonçalves M I & Walker A 2000 *Dysphagia* **15**(3), 146–152.

McClelland J, Hawkes D, Schaeffter T & King A 2013 *Medical Image Analysis* **17**(1), 19–42.

McClelland J R, Modat M, Arridge S, Grimes H, D'Souza D, Thomas D, Connell D O, Low D A, Kaza E, Collins D J, Leach M O & Hawkes D J 2017 *Physics in Medicine and Biology* **62**(11), 4273–4292.

Mulquiney J E, Norton J P, Jakeman A J & Taylor J A 1995 *Environmetrics* **6**(5), 473–478.

Mutic S & Dempsey J F 2014 *Seminars in Radiation Oncology* **24**(3), 196–199.

Nakata A, Tateoka K, Fujimoto K, Saito Y, Nakazawa T, Abe T, Yano M & Sakata K 2013 *International Journal of Medical Physics, Clinical Engineering and Radiation Oncology* **02**(04), 117–124.

Navest R, Bruijnen T, Lagendijk J, Andreychenko A & van den Berg C 2018 *in* 'Proc. Intl. Soc. Mag. Reson. Med. 26' Paris p. 702.

Navest R J M, Andreychenko A, Lagendijk J J W & van den Berg C A T 2018 *IEEE Transactions on Medical Imaging* **37**(8), 1751–1760.

Navest R J M, Mandija S, Bruijnen T, Stemkens B, Tijssen R H N, Andreychenko A, Lagendijk J J W & van den Berg C A T 2020 *Physics in Medicine & Biology* **65**(1), 01NT02.

Navest R, Mandija S, Andreychenko A, Raaijmakers A, Lagendijk J & van den Berg C 2019 *Magnetic Resonance in Medicine* .

Paganelli C, Portoso S, Garau N, Meschini G, Via R, Buizza G, Keall P, Riboldi M & Baroni G 2019 *Physics in Medicine & Biology* **64**(18), 185013.

Paganelli C, Whelan B, Peroni M, Summers P, Fast M, van de Lindt T, McClelland J, Eiben B, Keall P, Lomax T, Riboldi M & Baroni G 2018 *Physics in Medicine & Biology* **63**(22), 22TR03.

Prévost J B, de Boer H, Pöll J, Voet P & Levendag P 2008 *Radiotherapy and Oncology* **87**(2), 268–273.

Ruytenberg T, Verbist B M, Vonk-Van Oosten J, Astreinidou E, Sjögren E V & Webb A G 2018 *Frontiers in Oncology* **8**.

Stemkens B, Paulson E S & Tijssen R H N 2018 *Physics in Medicine & Biology* **63**(21), 21TR01.

Stemkens B, Tijssen R H N, de Senneville B D, Lagendijk J J W & van den Berg C A T 2016 *Physics in Medicine and Biology* **61**(14), 5335–5355.

Vahle T, Bacher M, Rigie D, Fenchel M, Speier P, Bollenbeck J, Schäfers K P, Kiefer B & Boada F E 2020 *Investigative Radiology* **55**(3), 153–159.

van Asselen B, Raaijmakers C P J, Lagendijk J J W & Terhaard C H J 2003 *International Journal of Radiation Oncology*Biology*Physics* **56**(2), 384–390.

van Heeswijk R B, Bonanno G, Coppo S, Coristine A, Kober T & Stuber M 2012 *Critical Reviews^{TM} in Biomedical Engineering* **40**(2), 99–119.

van Herk M, McWilliam A, Dubec M, Faivre-Finn C & Choudhury A 2018 *International Journal of Radiation Oncology*Biology*Physics* **101**(5), 1057–1060.

Zachiu C, Denis de Senneville B, Moonen C & Ries M 2015 *Medical Physics* **42**(7), 4137–4148.

Zachiu C, Papadakis N, Ries M, Moonen C & Denis de Senneville B 2015 *Physics in Medicine and Biology* **60**(23), 9003–9029.

Zhang B, Sodickson D K & Cloos M A 2018 *Nature Biomedical Engineering* **2**(8), 570–577.

Zhang G, Eddy Patuwo B & Y. Hu M 1998 *International Journal of Forecasting* **14**(1), 35–62.

Zijlema S E, Tijssen R H N, Malkov V N, van Dijk L, Hackett S L, Kok J G M, Lagendijk J J W & van den Berg C A T 2019 *Physics in Medicine & Biology* **64**(18), 185004.

Zijlema S, van Dijk L, Gotby L W, Italiaander M, Tijssen R H N, Lagendijk J J W & van den Berg C A T 2019 *in* '7th MR in RT Symposion' Toronto p. 23.